Editors' Suggestion

Probing Band Topology Using Modulational Instability

Daniel Leykam,[1,2,*] Ekaterina Smolina,[3] Aleksandra Maluckov,[1,4] Sergej Flach,[1,2] and Daria A. Smirnova[3,5]
[1]Center for Theoretical Physics of Complex Systems, Institute for Basic Science, Daejeon 34126, Korea
[2]Basic Science Program, Korea University of Science and Technology, Daejeon 34113, Korea
[3]Institute of Applied Physics, Russian Academy of Science, Nizhny Novgorod 603950, Russia
[4]P* Group, Vinča Institute of Nuclear Sciences, University of Belgrade, P.O. Box 522, 11001 Belgrade, Serbia
[5]Nonlinear Physics Centre, Australian National University, Canberra, Australian Capital Territory 2601, Australia

(Received 7 August 2020; accepted 13 January 2021; published 17 February 2021)

We analyze the modulational instability of nonlinear Bloch waves in topological photonic lattices. In the initial phase of the instability development captured by the linear stability analysis, long wavelength instabilities and bifurcations of the nonlinear Bloch waves are sensitive to topological band inversions. At longer timescales, nonlinear wave mixing induces spreading of energy through the entire band and spontaneous creation of wave polarization singularities determined by the band Chern number. Our analytical and numerical results establish modulational instability as a tool to probe bulk topological invariants and create topologically nontrivial wave fields.

DOI: 10.1103/PhysRevLett.126.073901

Topological photonic bands can be combined with appreciable mean-field nonlinear interactions in a variety of platforms [1–3], including exciton-polariton condensates in structured microcavities [4,5], waveguide arrays [6], metasurfaces [7], and ring resonators [8]. These nonlinear topological photonic systems are of growing interest due to not only potential applications such as lasers and optical isolators, but also their ability to host novel effects with no analog in electronic topological materials. For example, several previous studies have revealed the existence of self-localized wave packets such as edge and bulk solitons [9–16]. However, as the size of a soliton is determined by its total power, they require fine-tuned excitation conditions to create, making experiments challenging. It is therefore timely to unveil novel phenomena that can emerge *spontaneously* in nonlinear topological photonic systems, without requiring fine-tuning.

In this Letter, we study the nonlinear dynamics of Bloch waves in topological bands, establishing their sensitivity to topological invariants such as the Chern number. We show that the generic phenomenon of modulational instability can lead to the spontaneous formation of wave fields characterized by nontrivial Chern numbers inherited from the linear bands. The mechanism is the energy-dependent parametric gain provided by the modulational instability [17–24], which enables population of a single band starting from a simple plane wave initial state. In addition to providing a simple way to sculpture novel structured light fields, the modulational instability enables measurement of bulk topological invariants of bosonic wave systems. This is usually challenging unless the band eigenstates are known *a priori*, time-consuming Bloch band tomography is performed [25–28], or the bulk-edge correspondence is employed [29–31].

We first characterize the short time dynamics of nonlinear Bloch waves using the linear stability analysis. The Bloch waves at high symmetry points of the Brillouin zone exhibit a familiar long wavelength instability in the presence of weak nonlinearities, but they become stable at a critical nonlinearity strength. This critical strength coincides with the bifurcation of a nonlinear Dirac cone [32], where additional symmetry-breaking nonlinear Bloch waves emerge and their stability becomes sensitive to the band topology. Second, we use numerical simulations to study the modulational instability at longer propagation times. For weak nonlinearities, the instability remains confined to the initially excited band. Nonlinear wave mixing processes lead to the excitation of all the band's linear modes, imprinting the band's Chern number on the wave field's polarization [33,34]. Interestingly, the polarization field converges to a quasiequilibrium state well before the system thermalizes [35–38]. Thus, the topological properties of the band are imprinted on the modulational instability at small and large time and nonlinearity scales.

We consider a two-dimensional photonic lattice governed by the nonlinear Schrödinger equation

$$i\partial_t|\psi(\boldsymbol{r},t)\rangle = (\hat{H}_{\mathrm{L}} + \hat{H}_{\mathrm{NL}})|\psi(\boldsymbol{r},t)\rangle, \tag{1}$$

where t is the evolution variable (time or propagation distance), $|\psi(\boldsymbol{r},t)\rangle$ is the wave field profile, $\hat{H}_{\mathrm{L}}$ and $\hat{H}_{\mathrm{NL}}$ are linear and nonlinear parts of the Hamiltonian, and $\boldsymbol{r} = (x, y)$ indexes the lattice sites. We consider the chiral-π-flux model illustrated in Fig. 1(a). This is a two band tight binding model for a Chern insulator on a square lattice with two sublattices a and b, i.e., $|\psi\rangle = (\psi_a, \psi_b)^T$, described by the Bloch Hamiltonian [39]

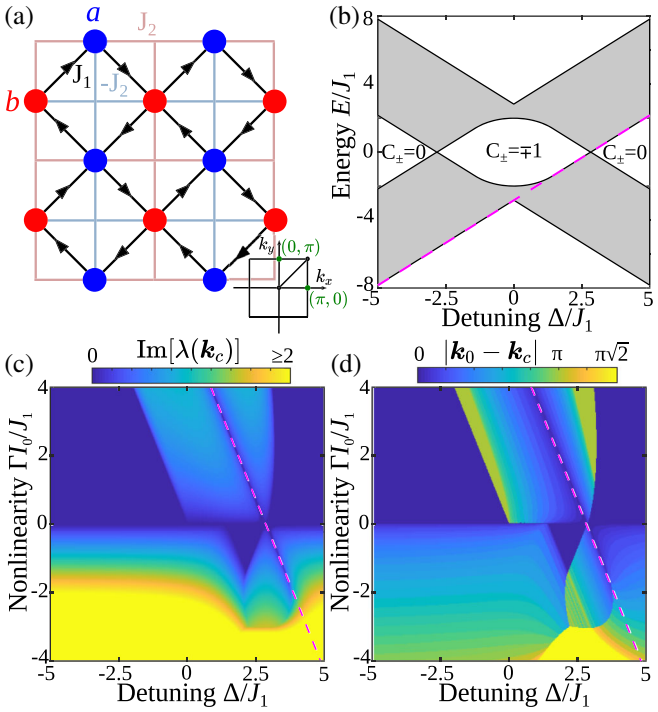

FIG. 1. Linear stability of the $\boldsymbol{k}_0 = (\pi, 0)$ nonlinear Bloch waves in the chiral-π-flux model. (a) Schematic of the lattice, consisting of two sublattices (a, b) with detuning Δ and inter (intra)sublattice couplings J_1 (J_2). Inset: the Brillouin zone. (b) Linear bands (shaded regions) characterized by Chern numbers $C_\pm$ as a function of Δ, for $J_2 = J_1/\sqrt{2}$. (c) Growth rate and (d) magnitude of the most unstable perturbation wave vector $\boldsymbol{k}_c$. Purple dashed line in (c),(d) marks the nonlinearity-induced gap closure at $\boldsymbol{k} = \boldsymbol{k}_0$, and the nonlinear Bloch wave is stable in the dark blue areas.

$$\hat{H}_{\mathrm{L}}(\boldsymbol{k}) = \boldsymbol{d}(\boldsymbol{k}) \cdot \hat{\boldsymbol{\sigma}}, \qquad d_z = \Delta + 2J_2(\cos k_x - \cos k_y),$$
$$d_x + i d_y = J_1[e^{-i\pi/4}(1 + e^{i(k_y - k_x)}) + e^{i\pi/4}(e^{-ik_x} + e^{ik_y})], \tag{2}$$

where the wave vector $\boldsymbol{k} = (k_x, k_y)$ is restricted to the first Brillouin zone $k_{x,y} \in [-\pi, \pi]$, $\hat{\boldsymbol{\sigma}} = (\hat{\sigma}_x, \hat{\sigma}_y, \hat{\sigma}_z)$ are Pauli matrices acting on the sublattice (pseudospin) degree of freedom, $J_{1,2}$ are nearest and next-nearest neighbor hopping strengths, and Δ is a detuning between the sublattices, which we use to tune between trivial and nontrivial topological phases. We will fix $J_2 = J_1/\sqrt{2}$, which enhances nonlinear effects by maximizing the band flatness [39]. For the nonlinear part of the Hamiltonian $\hat{H}_{\mathrm{NL}}$ we consider an on-site nonlinearity of the form

$$\hat{H}_{\mathrm{NL}} = \Gamma \mathrm{diag}[f(|\psi_a(\boldsymbol{r})|^2), f(|\psi_b(\boldsymbol{r})|^2)], \tag{3}$$

where Γ is the nonlinear interaction strength and f is the nonlinear response function, which describe the intensity dependence of the site energies.

The Bloch wave eigenstates of Eq. (2) form two energy bands $E_\pm(\boldsymbol{k})$, i.e., $\hat{H}_{\mathrm{L}}(\boldsymbol{k})|u_\pm(\boldsymbol{k})\rangle = E_\pm(\boldsymbol{k})|u_\pm(\boldsymbol{k})\rangle$. Figure 1(b) shows the spectrum of $\hat{H}_{\mathrm{L}}$, $E_\pm^2(\boldsymbol{k}, \Delta) = 4J_1^2[1 + \cos k_x \cos k_y] + [\Delta + 2J_2(\cos k_x - \cos k_y)]^2$, as a function of Δ/J_1, which exhibits topological phase transitions at $\Delta/J_1 = 2\sqrt{2}$ and $-2\sqrt{2}$, where the gap closes at one of the high symmetry points of the Brillouin zone $\boldsymbol{k}_0 = (\pi, 0)$ and $(0, \pi)$, respectively. The phase transitions correspond to changes in the quantized Chern numbers $C_\pm$, which is computed as the integral of the Bloch waves' Berry curvature over the Brillouin zone [40,41].

We focus on the nonlinear wave dynamics at the $\boldsymbol{k}_0 = (\pi, 0)$ high symmetry point. The linear Bloch wave can be continued as a nonlinear Bloch wave [42,43] $|\phi(\boldsymbol{r})\rangle = (\sqrt{I_0}, 0)^T e^{i\pi x}$ satisfying $(\hat{H}_{\mathrm{L}} + \hat{H}_{\mathrm{NL}})|\phi\rangle = E_{\mathrm{NL}}|\phi\rangle$, with energy $E_{\mathrm{NL}} = \Delta - 4J_2 + \Gamma f(I_0)$ bifurcating from the lower band when $\Delta < 4J_2$ and from the upper band when $\Delta > 4J_2$ [see purple line in Fig. 1(b)].

Performing the linear stability analysis, we consider the time evolution of a small perturbation to the steady state $|\phi\rangle$, $|\psi(t)\rangle = (|\phi\rangle + |\delta\phi(t)\rangle)e^{-iE_{\mathrm{NL}}t}$. By linearizing the equation of motion Eq. (1) about $|\phi\rangle$ we obtain an eigenvalue problem for the spectrum $\lambda(\boldsymbol{k})$ of perturbation modes $|\delta\phi(t)\rangle = |u\rangle e^{-i\lambda t} + |v^*\rangle e^{i\lambda^* t}$, which occur in complex conjugate pairs λ, λ^* due to the particle-hole symmetry of the linearized eigenvalue problem (see Supplemental Material [44] for details). Perturbations with growth rate $\mathrm{Im}(\lambda) > 0$ are linearly unstable. For the nonlinear response function, we consider pure Kerr nonlinearity $f(I) = I$; however, the qualitative features of the perturbation spectrum are insensitive to the precise form of $f(I)$ [44].

Figures 1(c) and 1(d) plot the growth rate and wave vector $\boldsymbol{k}_c$ of the most unstable perturbation mode, i.e., the mode with the maximum growth rate $\mathrm{Im}[\lambda(\boldsymbol{k}_c)] = \max_{\boldsymbol{k}} \mathrm{Im}[\lambda(\boldsymbol{k})]$, as a function of Δ and Γ. For weak nonlinearities Γ we observe behavior qualitatively similar to the scalar nonlinear Schrödinger equation: Bloch waves at the band edge exhibit a long wavelength instability under self-focusing nonlinearity, i.e., when $\Gamma m_{\mathrm{eff}} < 0$, where $m_{\mathrm{eff}} = \Delta - 4J_2$ is the wave effective mass at $\boldsymbol{k}_0$. Interestingly, a second long wavelength instability occurs for stronger nonlinearities in the vicinity of the stable line $\Gamma I_0/2 = -m_{\mathrm{eff}}$. This critical line occurs when the nonlinearity-induced potential closes the band gap and corresponds to a transition from an exponential instability at weak Γ to an oscillatory instability at strong Γ.

To reveal the generic behavior in the vicinity of the critical line, we consider the effective Dirac model obtained as a long wavelength expansion of Eq. (2), i.e., $\boldsymbol{k} = \boldsymbol{k}_0 + \boldsymbol{p}$ with $|\boldsymbol{p}| \ll 1$ [44],

$$\hat{H}_D = J_1\sqrt{2}(p_x\hat{\sigma}_y - p_y\hat{\sigma}_x) + (m_{\mathrm{eff}} + J_2[p_x^2 + p_y^2])\hat{\sigma}_z. \tag{4}$$

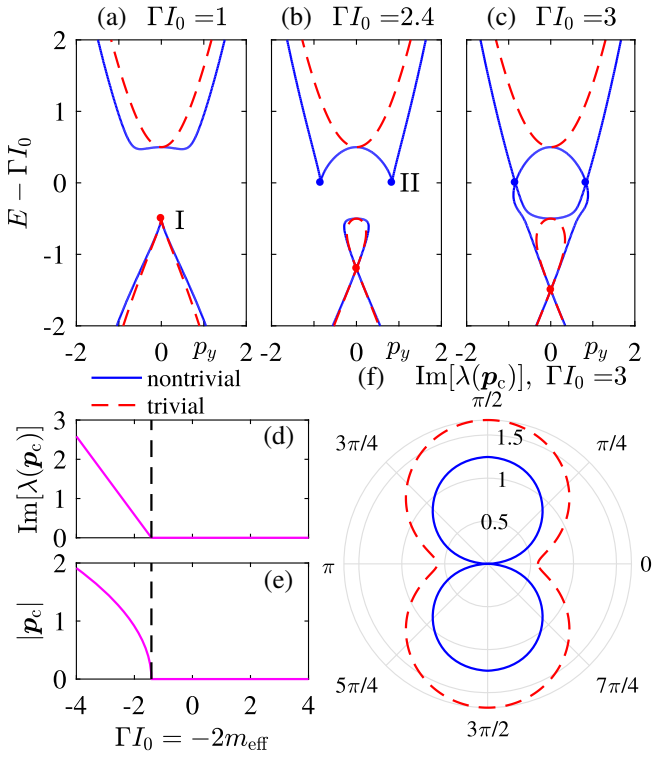

FIG. 2. (a)–(c) The transition in the nonlinear Bloch wave spectrum across the critical line in the nontrivial (solid blue, $m_{\mathrm{eff}} = -1/2$) and trivial (dashed red, $m_{\mathrm{eff}} = 1/2$) phases of the effective Dirac model (4). Colored dots mark special points in spectra with $p_y = 0, \pm p_{\mathrm{II}}$. (d) Growth rate and (e) magnitude of the most unstable perturbation wave vector along the critical line. (f) Instability growth rate as a function of the polar angle measured from the symmetry-breaking nonlinear Bloch wave vector in the nontrivial (solid blue) and trivial (dashed red) phases.

The quadratic $J_2[p_x^2 + p_y^2]\hat{\sigma}_z$ term is required to reproduce the correct Chern numbers $C_\pm = \pm\frac{1}{2}(1 - \mathrm{sgn}[J_2 m_{\mathrm{eff}}])$ [45] and the main features of perturbation spectrum.

The full nonlinear Bloch wave spectrum of Eq. (4) can be obtained analytically (see Supplemental Material [44]) and is shown in Figs. 2(a)–2(c). We observe that the critical line coincides with the formation of a nonlinear Dirac cone at $\boldsymbol{k}_0$, with $|\boldsymbol{p}| = p_{\mathrm{I}} = 0$ [32], i.e., a symmetry-breaking bifurcation [labeled I in Fig. 2(a)] of the nonlinear Bloch waves, which produces the linear band crossing in Fig. 2(b). At the bifurcation new modes $|\phi(\boldsymbol{r})\rangle = (\sqrt{I_a}e^{i\varphi}, \sqrt{I_b})e^{i\pi x}$ emerge, where both sublattices have nonzero intensities satisfying $I_0 = I_a + I_b$ and the relative phase between them φ forms a free parameter. Moreover, in the nontrivial phase ($C_\pm = \pm 1$, $|\Delta/J_1| < 2\sqrt{2}$), an additional bifurcation [labeled II in Fig. 2(b)] occurs at higher intensities at $|\boldsymbol{p}| = p_{\mathrm{II}} = \sqrt{4 - \Delta/J_2}$, corresponding to $d_z(\boldsymbol{p}) = 0$. The new branches emerging from this bifurcation merge with the lower band as ΓI_0 is increased [see Fig. 2(c)], producing a gapless nonlinear Bloch wave spectrum, while in the trivial phase ($C_\pm = 0$, $|\Delta/J_1| > 2\sqrt{2}$), the nonlinear Bloch wave spectrum remains gapped [44].

The nonlinear Dirac cone at $\boldsymbol{p} = 0$ occurs in both topological phases, but the modes' stability in the vicinity of the bifurcation point is sensitive to the linear band topology. For example, in both the tight binding and continuum models, the critical stable line terminates abruptly in the trivial phase at $\Delta = \Delta_c = 4J_2 + (J_1^2/2J_2)$, as shown in Figs. 2(d) and 2(e). Beyond this critical detuning, the most unstable wave vector is $|\boldsymbol{p}_c| = \sqrt{|\Gamma I_0 J_2 + J_1^2|/J_2^2}$; the length scale of the instability is dictated by the quadratic $J_2(p_x^2 + p_y^2)$ term and vanishes in the usual linear Dirac approximation, which neglects $p_{x,y}^2$ terms. As a second example, Fig. 2(f) shows the angular (directional) dependence of the maximal instability growth rate of the symmetry-breaking nonlinear Bloch wave. In the nontrivial phase, the instability is strongly anisotropic [44], with wave vectors in the direction perpendicular to the direction of the pseudospin remaining stable, whereas in the trivial phase, instabilities occur for all angles.

To understand these topological phase-dependent stability properties, we note that in the trivial phase the perturbation modes maintain a similar polarization to the nonlinear Bloch wave, enabling efficient nonlinear wave mixing and promoting instabilities. On the other hand, in the nontrivial phase, the perturbation modes' polarization rotates away to the opposite pole of the Bloch sphere, reducing the strength of the nonlinear wave mixing due to poor spatial overlap between the nonlinear Bloch wave and the perturbation modes [44]. While this difference may seem minor, it can play a critical role close to bifurcation points by lifting the degeneracy between the bands of perturbation modes. Thus, the modulational instability does not just depend on the energy eigenvalue dispersion, but is also sensitive to the geometrical properties of the Bloch waves, i.e., their polarization, and the band topology. This is our first key result.

Next, we carry out numerical simulations of Eq. (1) to study the modulational instability beyond the initial linearized dynamics. To characterize the complex multimode dynamics, we compute the following observables: (i) the normalized real space participation number, which measures the fraction of strongly excited lattice sites

$$P_r = \frac{\mathcal{P}^2}{2N}\left(\sum_{\boldsymbol{r}} |\psi_a(\boldsymbol{r})|^4 + |\psi_b(\boldsymbol{r})|^4\right)^{-1}, \tag{5}$$

where $\mathcal{P} = \sum_{\boldsymbol{r}} \langle\psi(\boldsymbol{r})|\psi(\boldsymbol{r})\rangle$ is the total power, (ii) the Fourier space participation number P_k, which measures similarly the fraction of excited Fourier modes, and (iii) the field polarization direction $\hat{\boldsymbol{n}}_\psi(\boldsymbol{k}) = \langle\psi(\boldsymbol{k})|\hat{\boldsymbol{\sigma}}|\psi(\boldsymbol{k})\rangle / \langle\psi(\boldsymbol{k})|\psi(\boldsymbol{k})\rangle$, which exhibits singularities sensitive to the band topology. We average these observables over an ensemble of small random initial

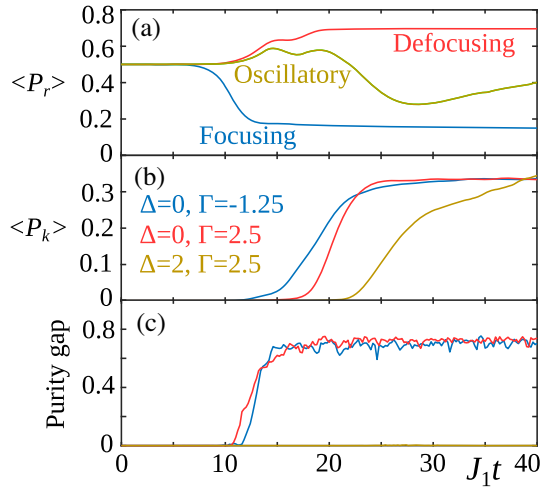

FIG. 3. Long time instability dynamics in the different instability regimes: focusing exponential (blue), defocusing exponential (red), and oscillatory instability (brown). (a) Real space participation number. (b) Fourier space participation number. (c) Purity gap.

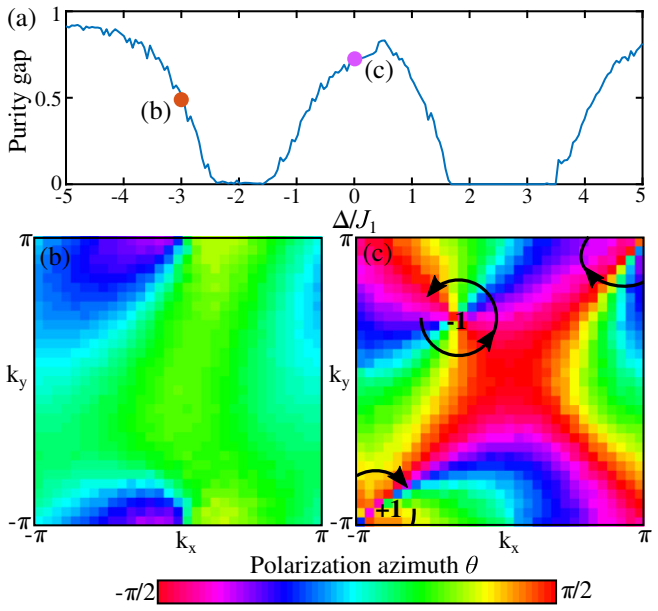

FIG. 4. (a) Purity gap at time $t = t_f = 40/J_1$ as a function of Δ. Field polarization textures at t_f in the (b) trivial ($\Delta = -3J_1$) and (c) nontrivial ($\Delta = 0$) phases. The Chern number is obtained by summing the charges of the polarization azimuth vortices (indicated by arrows) weighted by $\mathrm{sgn}(n_y)$ at the vortex core (indicated by ± 1) [33].

perturbations to the nonlinear Bloch wave. The average polarization $\langle \hat{\boldsymbol{n}}_\psi(\boldsymbol{k})\rangle$, in general, describes a mixed state with $n_\psi^2 = \langle \hat{\boldsymbol{n}}_\psi(\boldsymbol{k})\rangle \cdot \langle \hat{\boldsymbol{n}}_\psi(\boldsymbol{k})\rangle < 1$. When $n_\psi^2 > 0$ for all $\boldsymbol{k}$, i.e., the "purity gap" $\min_{\boldsymbol{k}}(n_\psi^2)$ remains open, the wave field is characterized by a quantized Chern number [46–48].

Figure 3 illustrates the dynamics of the $\boldsymbol{k}_0 = (\pi, 0)$ nonlinear Bloch wave with initial intensity $I_0 = 1$, when each lattice site is subjected to a random perturbation with amplitude not exceeding $0.01\sqrt{I_0}$. We use saturable nonlinearity of the form $f(I) = 2I/(1+I)$, which takes into account the inevitable saturation of nonlinear response at high intensities, a system size of $N = 32 \times 32$ unit cells with periodic boundary conditions [49], and average observables over 100 initial perturbations. We consider parameters corresponding to different instability regimes: exponential focusing, exponential defocusing, and oscillatory defocusing.

The focusing instability generates a collection of localized solitons, resulting in a decrease in $\langle P_r\rangle$ in Fig. 3(a). On the other hand, the defocusing nonlinearity spreads energy over both sublattices, resulting in a small increase in $\langle P_r\rangle$. In all cases, $\langle P_k\rangle$ increases due to other Fourier modes being populated via nonlinear wave mixing. For the exponential instabilities, this is accompanied by the purity gap opening and emergence of a well-defined Chern number corresponding to the band Chern number. Interestingly, the purity gap opens before $\langle P_{r,k}\rangle$ reach a steady state. Under the oscillatory instability, the purity gap remains negligible due to competition between pairs of instability modes with the same growth rates. Further details of the propagation dynamics in these different regimes may be found in the Supplemental Material [44].

To explore the emergence of a purity gap in more detail, we present in Fig. 4(a) its value at $t = t_f = 40J_1$ as a function of Δ, which tunes between the trivial and nontrivial phases [39]. For $\Delta > 0$, we observe good correspondence with the results of the linear stability analysis in Fig. 1: the size of the purity gap follows the instability growth rate, and the purity gap vanishes when the Bloch wave is linearly stable or exhibits an oscillatory instability, because the polarization becomes sensitive to the initial random perturbation. The purity gap also closes at $\Delta \approx -2J_1$, despite no change in the fastest growing instability mode, corresponding to a nonlinearity-induced closure of the band gap at $\boldsymbol{k} = (0, \pi)$.

While the trivial and nontrivial phases exhibit similar purity gaps, their differing topology can be observed by measuring the field polarization $\langle \hat{\boldsymbol{n}}_\psi(\boldsymbol{k})\rangle = (n_x, n_y, n_z)$ at long times, as illustrated in Figs. 4(b) and 4(c). In experiments, $\langle \hat{\boldsymbol{n}}_\psi(\boldsymbol{k})\rangle$ can be readily obtained by measuring the field's sublattice (spin) components in Fourier space; $n_z(\boldsymbol{k}) = (|\psi_a|^2 - |\psi_b|^2)/(|\psi_a|^2 + |\psi_b|^2)$ is the relative population imbalance between the two sublattices at $\boldsymbol{k}$, while $n_{x,y}$ depend on the relative phase between the two sublattices. Employing the method of Ref. [33], the Chern number can hence be obtained by summing the charges of the phase singularities of the polarization azimuth $\theta = \frac{1}{2}\tan^{-1}(n_x/n_z)$ weighted by $\mathrm{sgn}(n_y)$. In the trivial phase (large Δ), the field is predominantly localized to a single sublattice, such that n_z remains nonzero and there are no phase singularities in θ; hence $C = 0$. In the nontrivial phase, $\langle \hat{\boldsymbol{n}}_\psi(\boldsymbol{k})\rangle$ spans the entire Bloch sphere, corresponding to a pair of opposite charge phase singularities with

opposite weights $\mathrm{sgn}(n_y) = \pm 1$, and hence $C = 1$. Thus, the long time instability dynamics can be used to measure the band Chern number. This is our second important finding.

In conclusion, we have studied how the modulational instability of nonlinear Bloch waves can be used to probe band topology. The linear stability spectrum describing the short time instability dynamics exhibits bifurcations and a reemergence of stability, which are sensitive to topological band inversions. At longer evolution times, nonlinear wave mixing can populate an entire band, enabling the spontaneous creation of topologically nontrivial wave fields from simple plane wave initial states. Since the timescales involved are shorter than the wave thermalization time, these effects should be experimentally observable in nonlinear waveguide arrays [6], Bose-Einstein condensates in optical lattices [22,23], or exciton-polariton condensates [4,5]. While we focused on the chiral-π-flux model, we have observed similar behavior in other topological tight binding models. Lattices with a larger band flatness typically exhibit emergence of a purity gap and well-defined Chern number for a wider range of nonlinearity strengths. It will be interesting to generalize our findings to periodically driven Floquet systems such as the nonlinear waveguide array employed in Ref. [6], where perfectly flat topological bands have been demonstrated.

We thank Mikael Rechtsman for illuminating discussions. This research was supported by the Institute for Basic Science in Korea (IBS-R024-Y1, IBS-R024-D1), the Australian Research Council Early Career Researcher Award (DE190100430), and the Ministry of Education, Science, and Technological Development of the Republic of Serbia. Theoretical analysis of the continuum model was supported by the Russian Science Foundation (Grant No. 20-72-00148).

*Present address: Centre for Quantum Technologies, National University of Singapore, 3 Science Drive 2, Singapore 117543.

[1] T. Ozawa *et al.*, Topological photonics, Rev. Mod. Phys. **91**, 015006 (2019).

[2] D. Smirnova, D. Leykam, Y. D. Chong, and Y. Kivshar, Nonlinear topological photonics, Appl. Phys. Rev. **7**, 021306 (2020).

[3] A. Saxena, P. G. Kevrekidis, and J. Cuevas-Marave, Nonlinearity and topology, in *Emerging Frontiers in Nonlinear Science. Nonlinear Systems and Complexity*, edited by P. Kevrekidis, J. Cuevas-Maraver, and A. Saxena (Springer, Cham, 2020), Vol. 32, pp. 25–54, https://doi.org/10.1007/978-3-030-44992-6_2.

[4] S. Klembt *et al.*, Exciton-polariton topological insulator, Nature (London) **562**, 552 (2018).

[5] F. Baboux *et al.*, Unstable and stable regimes of polariton condensation, Optica **5**, 1163 (2018).

[6] S. Mukherjee and M. C. Rechtsman, Observation of Floquet solitons in a topological bandgap, Science **368**, 856 (2020).

[7] D. Smirnova, S. Kruk, D. Leykam, E. Melik-Gaykazyan, D.-Y. Choi, and Y. Kivshar, Third-Harmonic Generation in Photonic Topological Metasurfaces, Phys. Rev. Lett. **123**, 103901 (2019).

[8] S. Mittal, E. A. Goldschmidt, and M. Hafezi, A topological source of quantum light, Nature (London) **561**, 502 (2018).

[9] M. J. Ablowitz, C. W. Curtis, and Y.-P. Ma, Linear and nonlinear traveling edge waves in optical honeycomb lattices, Phys. Rev. A **90**, 023813 (2014).

[10] Y. Lumer, M. C. Rechtsman, Y. Plotnik, and M. Segev, Instability of bosonic topological edge states in the presence of interactions, Phys. Rev. A **94**, 021801(R) (2016).

[11] Y. V. Kartashov and D. V. Skryabin, Modulational instability and solitary waves in polariton topological insulators, Optica **3**, 1228 (2016).

[12] D. Leykam and Y. D. Chong, Edge Solitons in Nonlinear Photonic Topological Insulators, Phys. Rev. Lett. **117**, 143901 (2016).

[13] Y. Lumer, Y. Plotnik, M. C. Rechtsman, and M. Segev, Self-Localized States in Photonic Topological Insulators, Phys. Rev. Lett. **111**, 243905 (2013).

[14] A. N. Poddubny and D. A. Smirnova, Ring Dirac solitons in nonlinear topological systems, Phys. Rev. A **98**, 013827 (2018).

[15] J. L. Marzuola, M. Rechtsman, B. Osting, and M. Bandres, Bulk soliton dynamics in bosonic topological insulators, arXiv:1904.10312.

[16] D. A. Smirnova, L. A. Smirnov, D. Leykam, and Y. S. Kivshar, Topological edge states and gap solitons in the nonlinear Dirac model, Laser Photonics Rev. **13**, 1900223 (2019).

[17] V. E. Zakharov and L. A. Ostrovsky, Modulation instability: The beginning, Physica (Amsterdam) **238D**, 540 (2009).

[18] R. W. Boyd, *Nonlinear Optics* (Academic Press, New York, 2008).

[19] Y. S. Kivshar and M. Peyrard, Modulational instabilities in discrete lattices, Phys. Rev. A **46**, 3198 (1992).

[20] G. Engelhardt and T. Brandes, Topological Bogoliubov excitations in inversion-symmetric systems of interacting bosons, Phys. Rev. A **91**, 053621 (2015).

[21] C.-E. Bardyn, T. Karzig, G. Refael, and T. C. H. Liew, Chiral Bogoliubov excitations in nonlinear bosonic systems, Phys. Rev. B **93**, 020502(R) (2016).

[22] P. J. Everitt *et al.*, Observation of a modulational instability in Bose-Einstein condensates, Phys. Rev. A **96**, 041601(R) (2017).

[23] J. H. V. Nguyen, D. Luo, and R. G. Hulet, Formation of matter-wave soliton trains by modulational instability, Science **356**, 422 (2017).

[24] K. Lelas, O. Čelan, D. Prelogović, H. Buljan, and D. Jukić, Modulation instability in the nonlinear Schrödinger equation with a synthetic magnetic field: Gauge matters, Phys. Rev. A **103**, 013309 (2021).

[25] C.-E. Bardyn, S. D. Huber, and O. Zilberberg, Measuring topological invariants in small photonic lattices, New J. Phys. **16**, 123013 (2014).

[26] M. Aidelsburger, M. Lohse, C. Schweizer, M. Atala, J. T. Barreiro, S. Nascimbène, N. R. Cooper, I. Bloch, and N. Goldman, Measuring the Chern number of Hofstadter bands with ultracold bosonic atoms, Nat. Phys. **11**, 162 (2015).
[27] M. Wimmer, H. M. Price, I. Carusotto, and U. Peschel, Experimental measurement of the Berry curvature from anomalous transport, Nat. Phys. **13**, 545 (2017).
[28] M. Tarnowski, F. N. Ünal, N. Fläschner, B. S. Rem, A. Eckardt, K. Sengstock, and C. Weitenberg, Measuring topology from dynamics from obtaining the Chern number from a linking number, Nat. Commun. **10**, 1728 (2019).
[29] A. V. Poshakinskiy, A. N. Poddubny, and M. Hafezi, Phase spectroscopy of topological invariants in photonic crystals, Phys. Rev. A **91**, 043830 (2015).
[30] W. Hu, J. C. Pillay, K. Wu, M. Pasek, P. P. Shum, and Y. D. Chong, Measurement of a Topological Edge Invariant in a Microwave Network, Phys. Rev. X **5**, 011012 (2015).
[31] S. Mittal, S. Ganeshan, J. Fan, A. Vaezi, and M. Hafezi, Measurement of topological invariants in a 2D photonic system, Nat. Photonics **10**, 180 (2016).
[32] R. W. Bomantara, W. Zhao, L. Zhou, and J. Gong, Nonlinear Dirac cones, Phys. Rev. B **96**, 121406(R) (2017).
[33] T. Fösel, V. Peano, and F. Marquardt, *L* lines, *C* points and Chern numbers: Understanding band structure topology using polarization fields, New J. Phys. **19**, 115013 (2017).
[34] D. Leykam and D. A. Smirnova, Probing bulk topological invariants using leaky photonic lattices, Nat. Phys. (2021), https://doi.org/10.1038/s41567-020-01144-5.
[35] P. Buonsante, R. Franzosi, and A. Smerzi, Phase transitions at high energy vindicate negative microcanonical temperature, Phys. Rev. E **95**, 052135 (2017).
[36] T. Mithun, Y. Kati, C. Danieli, and S. Flach, Weakly Nonergodic Dynamics in the Gross-Pitaevskii Lattice, Phys. Rev. Lett. **120**, 184101 (2018).
[37] M. Hafezi, P. Adhikari, and J. M. Taylor, Chemical potential for light by parametric coupling, Phys. Rev. B **92**, 174305 (2015).
[38] F. O. Wu, A. U. Hassan, and D. N. Christodoulides, Thermodynamic theory of highly multimoded nonlinear optical systems, Nat. Photonics **13**, 776 (2019).
[39] T. Neupert, L. Santos, C. Chamon, and C. Mudry, Fractional Quantum Hall States at Zero Magnetic Field, Phys. Rev. Lett. **106**, 236804 (2011).
[40] M. Z. Hasan and C. L. Kane, Colloquium: Topological insulators, Rev. Mod. Phys. **82**, 3045 (2010).
[41] D. Xiao, M.-C. Chang, and Q. Niu, Berry phase effects on electronic properties, Rev. Mod. Phys. **82**, 1959 (2010).
[42] D. Träger, R. Fischer, D. N. Neshev, A. A. Sukhorukov, C. Denz, W. Królikowski, and Y. S. Kivshar, Nonlinear Bloch modes in two-dimensional photonic lattices, Opt. Express **14**, 1913 (2006).
[43] Y. V. Kartashov, B. A. Malomed, and L. Torner, Solitons in nonlinear lattices, Rev. Mod. Phys. **83**, 247 (2011).
[44] See Supplemental Material at http://link.aps.org/supplemental/10.1103/PhysRevLett.126.073901 which contains details of the linear stability analysis, calculation of the nonlinear Bloch wave spectrum, and simulations of the instability dynamics. In Sec. 2, we provide a justification of the perturbation modes maintaining a similar polarization for weak nonlinearities. In Sec. 3.2, we plot examples of the perturbation modes' wave-vector-dependent spin and polarization in the trivial and nontrivial phases.
[45] S.-Q. Shen, *Topological Insulators. Dirac Equation in Condensed Matters* (Springer, New York, 2012).
[46] Y. Hu, P. Zoller, and J. C. Budich, Dynamical Buildup of a Quantized Hall Response from Nontopological States, Phys. Rev. Lett. **117**, 126803 (2016).
[47] C.-E. Bardyn, M. A. Baranov, C. V. Kraus, E. Rico, A. Imamoglu, P. Zoller, and S. Diehl, Topology by dissipation, New J. Phys. **15**, 085001 (2013).
[48] J. C. Budich and S. Diehl, Topology of density matrices, Phys. Rev. B **91**, 165140 (2015).
[49] Alternatively, one could use a finite lattice superimposed with a sufficiently broad trapping potential.